The Impact of Choice of Solar Spectral Irradiance Model on Atmospheric Correction of Landsat 8 OLI Satellite Data

Fuqin Li, *Senior Member, IEEE*, David L. B. Jupp, *Life Member, IEEE,* Stephen Sagar, and Thomas Schroeder

***Abstract*— Many atmospheric correction schemes of radiance-based optical satellite data require the selection of normalized solar spectral irradiance models at the top of atmosphere (TOA). However, there is no scientific consensus in literature as to which available model is most suitable. This article examines five commonly used models applied to Landsat 8 Operational Land Imager (OLI) TOA radiance and reflectance products to assess the accuracy and stability between models used to derive surface reflectance products. It is assumed that the calibration of the United States Geological Survey (USGS) Landsat 8 OLI TOA reflectance and radiance products are accurate to currently claimed levels. The results show that the retrieved surface reflectance can exhibit significant variations when different solar irradiance models are used, especially in the OLI coastal blue band at 443 nm. From the five solar irradiance models, the Kurucz 2005 model showed the least bias compared with OLI TOA reflectance product and least variance in surface reflectance. Furthermore, improvement was obtained by adjusting the total solar irradiance (TSI) normalization, and additional validation was provided using observed *in situ* water leaving reflectance data. The results from this article are particularly relevant to aquatic applications and to satellite sensors that provide TOA radiance such as previous Landsat and other current and historical missions.**

***Index Terms*— Atmospheric correction, Landsat 8 Operational Land Imager (OLI), sensor calibration, solar irradiance, spectral solar constant.**

I. Introduction and Background

THE normalized solar spectral irradiance at the top of atmosphere (TOA) is an important boundary condition used in radiative transfer modeling as well as energy balances of the atmosphere [1]. It is a fundamental observation used in a wide range of applications ranging from climate modeling [2] to atmospheric correction of satellite data, where the sensors measure upwelling radiance resulting from interactions with atmosphere and the Earth's surface [3]–[5]. For Earth observation applications, its shape and magnitude are particularly important for spectral wavelengths less than 500 nm, where spectral variations in the solar irradiance flux are larger compared to longer wavelength. The total integrated energy over all wavelengths varies periodically with the Sun–Earth distance, and its value normalized to the mean Sun–Earth distance is called the solar constant. The solar spectral irradiance normalized to mean Sun–Earth distance has sometimes been called the "spectral solar constant," a term which will be used here to avoid confusion with other irradiances. The integrated value over all wavelengths is the "total solar irradiance" (TSI). The TSI also varies over time with the 11-year cycle of solar activity, but it is a relatively small variation [2], [6] compared with the annual Sun–Earth distance effect with only about a 0.5% variation occurring in the visible and near-infrared (NIR) areas of the spectrum [2]. The structure and form of the spectral solar constant have been the focus of intensive and long-term studies incorporating ground and satellite observations, leading to the existence of a number of published estimates covering a wide range of wavelengths relevant to Earth observation at very high spectral resolutions [3]–[5], [7].

Despite the observed low variability (other than Sun–Earth distance) of the spectral solar constant in spectral regions used for recent Earth observation (roughly 400–2600 nm), it has been observed that there are considerable differences between the commonly available estimates. For example, Zhang *et al.* [8] studied the effects of using selections of spectral solar constant from six older models and found significant differences in the calculation of indices. They suggested the Thuillier model [4] seemed to be most accurate but found it hard to evaluate what establishes a "best" model. Thome *et al.* [9] made a more detailed comparison with two selections of spectral solar constant in regards to the vicarious calibrations of instruments prior to Landsat 8. They concluded that the differences existed, and one (the Chance and Kurucz 1997 model [7]) seemed better than the other. However, they suggested that vicarious calibration bias would have to be less than 5% to provide a proper assessment. Similarly with [9], Shanmugam and Ahn [10] addressed the same questions for ocean color situations and identified significant effects in the low reflectance targets. However, they also found vicarious methods not accurate enough to decide between the choices of calibration and spectral solar constant selection. Their preference was the Thuillier model [4].

Manuscript received August 26, 2019; revised February 10, 2020; accepted July 6, 2020. Date of publication August 6, 2020; date of current version April 22, 2021. This work was supported by the Geoscience Australia. Australian Integrated Marine Observing System (IMOS) and Commonwealth Scientific and Industrial Research Organization (CSIRO) are acknowledged for funding the Lucinda AERONET-OC site. *(Corresponding author: Fuqin Li.)*

Fuqin Li and Stephen Sagar are with National Earth and Marine Observations Branch, Environmental Geoscience Division, Geoscience Australia, Canberra, ACT 2601, Australia (e-mail: fuqin.li@ga.gov.au; stephen.sagar@ga.gov.au).

David L. B. Jupp is with CSIRO Land and Water, Canberra, ACT 2601, Australia (e-mail: david.jupp@csiro.au).

Thomas Schroeder is with CSIRO Oceans and Atmosphere, Brisbane, QLD 4001, Australia (e-mail: thomas.schroeder@csiro.au).

Color versions of one or more of the figures in this article are available online at https://ieeexplore.ieee.org.

Digital Object Identifier 10.1109/TGRS.2020.3011006

Landsat 8 OLI data can possibly resolve the questions left unanswered by the previous studies. The data have a very high signal-to-noise ratio (SNR) and radiometric stability [11] compared with previous Landsat instruments and are provided to end users as both calibrated TOA reflectance and TOA radiance products. These products are based on two different calibration approaches [11]. The TOA radiance product employs traditional direct calibration of the observed radiance using prelaunch laboratory calibration maintained by on-board lamps as well as innovative methods such as lunar observations and other cross-checks. For the TOA reflectance product, the measurement is directly referenced to solar irradiance using solar diffuser panels. Regular measurements are interpolated to a particular scene using Sun–Earth distance variations. It is theoretically an ideal way to calculate the TOA reflectance as the radiative transfer-based atmospheric correction process in this case does not then require a reference spectral solar constant model from the literature. As the panel reading senses the "true" solar irradiance, the comparison between the retrieved surface reflectance using TOA radiance and TOA reflectance also provides an opportunity to evaluate how different solar constant models perform in atmospheric correction, assuming the accurate calibration of both OLI TOA radiance and reflectance.

In this article, five commonly used solar constant models and one normalized model generated as part of this work have been used to evaluate their suitability for operational atmospheric correction of OLI data. The models include three of 13 available in MODTRAN 6 [7], along with one from the open-source software version of 6S [12], and one based on Thuillier *et al.* [4], currently recommended for standard use in atmospheric correction for Earth observation by CEOS [13]. The motivation for this study was to quantify the variation seen in retrieved surface reflectance using different selections of spectral solar constant models and TOA radiance. In particular, considerable differences had been observed in water covered areas and dense vegetation in the new coastal blue spectral band (433–453 nm) available for Landsat 8 OLI. The previous studies have proposed that either the coastal blue bands were not well calibrated [14], or as is being considered here, there was a problem with the spectral solar constant.

II. Methods, Data, and Study Areas

A. Methods

TOA reflectance can be defined as follows:

$$\rho_{\text{toa}} = \frac{\pi L_{\text{toa}} d^2}{E_0 \cos(\theta_s)} = \frac{\pi L_{\text{toa}}}{E_0^{'} \cos(\theta_s)} \tag{1}$$

where L_{toa} is radiance measured by the sensor, E_0 is the spectral solar constant at the TOA for mean Sun–Earth distance, E_0' is estimated normal solar irradiance at the TOA for the Sun–Earth distance at the time of measurement, d is the ratio of Sun–Earth distance to mean Sun–Earth distance (astronomical units), and θ_s is the solar zenith angle.

Since the spectral solar irradiance is incorporated into atmospheric correction primarily through the magnitudes of surface irradiance and path radiance terms, the Lambertian surface reflectance ρ_s estimate can be used to analyze the impact of the spectral solar constant. For a given waveband, Lambertian surface reflectance ρ_s can be written as follows:

$$\rho_s = \frac{(L_{\text{toa}} - L_p)}{E_0^{'} \cos(\theta_s) T_v T_s / \pi + S(L_{\text{toa}} - L_p)} \tag{2}$$

where L_p is path radiance added by the atmosphere, T_s and T_v are total transmittances of the sun and view directions, respectively, and S is atmospheric albedo (accounting for interactions between surface and atmosphere). In this article, the terms of (2) are provided by running MODTRAN [7] at wavenumber level to solve the radiative transfer and balance energy. The properly integrated terms (such as transmittances or albedos) at spectral band level allow (2) to be used for band data with high accuracy. The spectral solar constant is also applied at wavenumber level, and its integrated band value is output by MODTRAN [7]. MODTRAN allows a user to provide their preferred spectral solar constant model when it is not available from standard selections. The terms used in this article are all assumed to be integrated correctly to the seven Landsat 8 bands. However, the band dependence is suppressed to keep the expressions simpler.

Using (1), L_{toa} can be expressed as $\rho_{\text{toa}} E_0' \cos(\theta_s)/\pi$, and if L_p can also expressed as $\rho_p E_0' \cos(\theta_s)/\pi$, (2) can be expressed as

$$\rho_s = \frac{\rho_{\text{toa}} - \rho_p}{T_v T_s + S(\rho_{\text{toa}} - \rho_p)}. \tag{3}$$

In (3), ρ_p is path reflectance which is effectively independent of solar irradiance and can be defined as $\pi L_p / (E_0' \cos(\theta_s))$. Strictly, ρ_p is only independent of E_0' at single wavelength or wavenumber level. However, if integrated properly, any difference at band level is negligible. Equation (3), therefore, shows that to very close approximation, the retrieval of band integrated (Lambertian) surface reflectance ρ_s does not require the selection of a spectral solar constant model if the satellite sensor measures ρ_{toa} directly.

Most of the sensors only provide measured TOA radiance, and thus, the accuracy of the retrieved surface reflectance depends on the effective selection of a spectral solar constant model. Since OLI has independent calibrated TOA radiance and TOA reflectance products [11], the comparison between the retrieved surface reflectance from TOA radiance and TOA reflectance can be used to evaluate the performance of the spectral solar constant model used in the correction.

To demonstrate how the choice of spectral solar constant affects the retrieval of Lambertian surface reflectance, the term ρ_s can be replaced by a term ρ_s' defined as $\rho_s' = \rho_s/(1 - S\rho_s)$ to simplify the equations. The relationship between ρ_s and ρ_s' is very close, and converting between them does not involve the choice of solar constant. With this change and combined with (1), (3) can then be written more concisely as

$$\rho_{\text{toa}} = T_v T_s \rho'_s + \rho_p = \frac{\pi L_{\text{toa}}}{E_0^{'} \cos(\theta_s)}. \tag{4}$$

Consider that there are two selections of solar constant, namely, Case 1 and Case 2. Both are assumed adjusted for the Sun–Earth distance and are, therefore, denoted E_{01}' and E_{02}', respectively. In this article, Case 1 will be taken as for

OLI when ρ_{toa} has been estimated directly from the TOA reflectance product. Assume that the panel reflectance for TOA reflectance is accurately known, and then, the solar irradiance for Case 1 is a measured value. Case 2 uses a selected spectral solar constant model and the OLI TOA radiance product. In both cases, the radiance (L_{toa}) will be the same if the OLI calibrations for both TOA reflectance and TOA radiance products are accurate. Then, reformatting (4) leads to

$$\begin{aligned} L_{\text{toa}} &= \frac{1}{\pi} E_{01}^{'} \cos(\theta_s)\left(T_v T_s \rho_{s1}' + \rho_p\right) \\ &= \frac{1}{\pi} E_{02}^{'} \cos(\theta_s)\left(T_v T_s \rho_{s2}' + \rho_p\right). \end{aligned} \tag{5}$$

In this equation, ρ_{s1}' and ρ_{s2}' are retrieved Lambertian surface reflectance factors (or strictly the composite factors involving S) for Case 1 and Case 2, respectively.

The ratio of the TOA reflectance values (r_t) from the two cases is defined from (1) as

$$r_t = \frac{\rho_{\text{toa2}}}{\rho_{\text{toa1}}} = \frac{E_{01}}{E_{02}} = \frac{E_{01}^{'}}{E_{02}^{'}} \tag{6}$$

where ρ_{toa1} and ρ_{toa2} are TOA reflectance values for Case 1 and Case 2, respectively. Note that although the value of E_{01} is not explicitly known, the ratio (r_t) can still be found. This ratio is found to be very stable and is only waveband dependent.

Rewriting (5), it follows that

$$\rho_{s2}' = r_t \rho_{s1}' + (r_t - 1)\frac{\rho_p}{T_v T_s} = r_t \rho_{s1}' + (r_t - 1)\rho_p^*. \tag{7}$$

This relates the reflectance that is obtained if the selected spectral solar constant model and TOA radiance are used (ρ_{s2}') to the solution obtained if the TOA reflectance product is used (ρ_{s1}'). Obviously, if $r_t = 1$, then the two cases result in the same ground target value. In this article, ρ_{s1}' will be taken as the correct result. Otherwise, the result of using the spectral solar constant model is altered by the ratio r_t and a bias term denoted ρ_p^* which depends on the path radiance, diffuse radiation, and transmittances. The bias term is greatest in the blue and least in the NIR and shortwave infrared (SWIR).

This result can be expressed in other ways. One way is as the difference between the values

$$\rho_{s2}' - \rho_{s1}' = (r_t - 1)\left(\rho_{s1}' + \rho_p^*\right). \tag{8}$$

The difference is depending on land cover (ρ_{s1}') and the bias term (ρ_p^*).

Another way to evaluate the change is to use the ratio

$$r_s = \frac{\rho_{s2}'}{\rho_{s1}'} = r_t + (r_t - 1)\frac{\rho_p^*}{\rho_{s1}'}. \tag{9}$$

The result is that surface ratio r_s is the ratio of TOA reflectance values (r_t) plus a perturbation consisting of the ratio of the new wavelength-dependent bias term (ρ_p^*) and the Case 1 surface target reflectance.

Based on this theoretical model (9), it is clear that low reflectance targets are more greatly affected in the shorter wavelength regions. Thus, these effects have been noticed in aquatic applications, where even small variations can lead to an unrealistic spectral signature for techniques utilizing radiative transfer or physics-based methods with a radiance product.

TABLE I
SPECTRAL SOLAR CONSTANT MODELS TESTED IN THE STUDY

Model	References
1	MODTRAN 6 default, MODTRAN LSUNFL default [3] [7]
2	Kurucz 2005, MODTRAN LSUNFL 1 [5] [7]
3	MODTRAN Thuillier, MODTRAN LSUNFL 4 [7]
4	Open source 6S [12]
5	CEOS Thuillier [13]
6	Normalised Kurucz 2005 (Model 2) [5] [7] scaled by a factor of 0.988

B. Data and Study Area

Six solar constant models have been used in this study as the Case 2 selections, and they are shown in Table I.

The Model 6 is the Kurucz 2005 (Model 2) adjusted to have the average ratio (r_t) over spectral bands nearer to 1.0, as described later.

The atmospheric and surface radiometric measurements are routinely collected at the Integrated Marine Observing System (IMOS) Lucinda Jetty Coastal Observatory (LJCO) located at the end of a 6 km long jetty in coastal waters of the Great Barrier Reef south of Hinchinbrook Island, Queensland. The LJCO operates a modified version of a CIMEL CE-318 sun-photometer, capable of performing autonomous atmospheric and above water radiance measurements at defined viewing and azimuth angles. This system contributes to NASA's global AERONET-OC network [15]. During clear-sky conditions, the instrument measures the water-leaving radiance at approximately half hourly intervals in eight spectral bands between 412 and 1018 nm. These measurements are available for ground validation. Direct sun and sky radiance measurements are also performed to derive spectral columnar aerosol optical depth and additional products such as precipitable water vapor. The OLI tile covering LJCO (18.52 S, 146.39 E) and defined by path 095 and row 073 also includes other land and ocean surfaces without field measurements but with atmospheric information provided by the LJCO. These sites are also suitable for testing the impact of the spectral solar irradiance models. Fig. 1 shows the false color image of Lucinda and surrounding areas. The yellow stars are the 15 land cover sites without ground truth data that are used for the general analysis later. The targets include rainforest, agriculture, inland and ocean water, and mangrove and bare soil. Table II shows the 11 selected Landsat 8 images that have concurrent LJCO and land cover observations acquired during different seasons and years.

The images were processed in two groups to calculate Lambertian surface reflectance using (2) and (3) and the OLI TOA reflectance and radiance products. Since it is time consuming and impractical to run MODTRAN pixel by pixel, in this study, Landsat images were divided into four rectangles and MODTRAN run at the nine corner coordinates. For any pixel in the image, the MODTRAN outputs are then interpolated from the nine points using bilinear interpolation in each rectangle to get the pixel values [16]. These can account for multiangle effects in the atmosphere. Since Australia

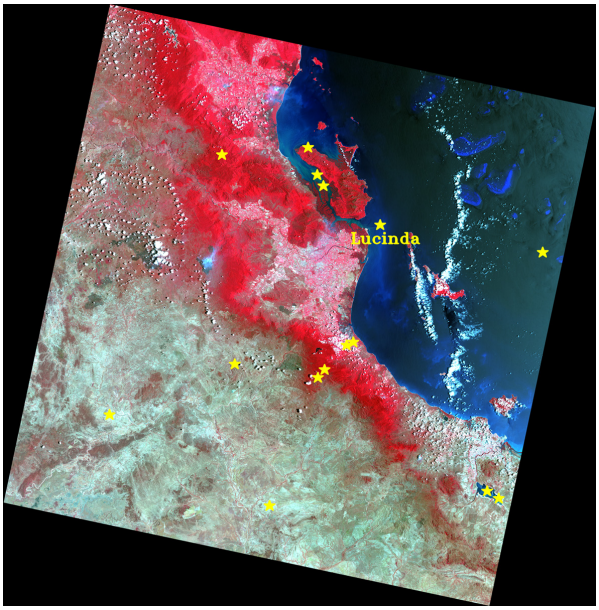

Fig. 1. False color image of test scene, where yellow stars are the test sites and the star beside Lucinda is the LJCO.

TABLE II
LANDSAT 8 DATA USED IN THIS ARTICLE

Date (dd/mm/year)	Scene centre information (path 095, row 073) Time (H) (UTC)	Latitude (°)	Longitude (°)
03/01/2014	0.3031	18.7902S	146.0873E
28/06/2014	0.2756	18.7903S	146.1035E
31/08/2014	0.2817	18.7904S	146.0985E
16/09/2014	0.2825	18.7903S	146.0993E
02/10/2014	0.2829	18.7903S	146.1010E
18/10/2014	0.2841	18.7901S	146.0880E
19/11/2014	0.2831	18.7903S	146.1019E
18/08/2015	0.2757	18.7902S	146.0979E
21/10/2015	0.2811	18.7903S	146.0968E
26/02/2016	0.2784	18.7904S	146.1086E
10/10/2017	0.2848	18.7904S	146.0794E

has little spatial variation of aerosol and water vapor, single aerosol and precipitable water vapor for Landsat scene extent (200 km × 200 km) were used, and the data were obtained from the AERONET web site [17] and other ancillary data were from the Geoscience Australia Analysis Ready Data (ARD) processing system [16]. Only r_s is impacted by atmosphere based on (6) and (9).

III. RESULTS

All 11 images were processed to Lambertian surface reflectance using the TOA reflectance product as well as the TOA radiance product and with the six spectral solar constant models shown in Table I. To assess the impacts on the surface reflectance retrieval, the coordinates of the 15 target areas with various landcover types (inland water, ocean water, agriculture, rainforest, bare soil and mangrove, etc.) were identified in each image (the yellow stars in Fig. 1), and a kernel of 9 × 9 pixels was used for each site to average both TOA and surface reflectance.

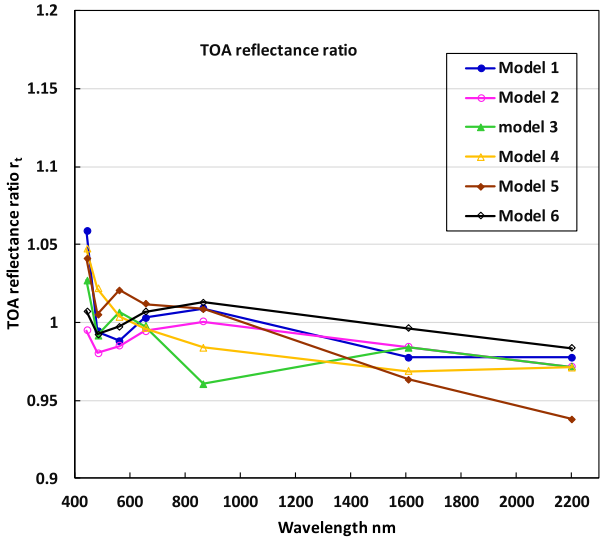

Fig. 2. Average TOA reflectance ratio, r_t.

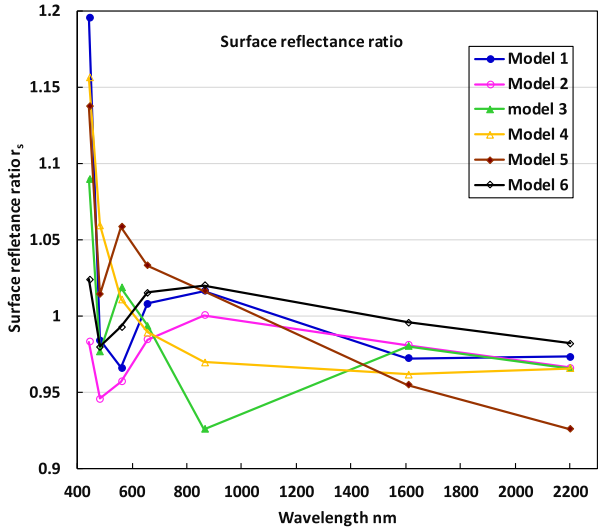

Fig. 3. Average surface reflectance ratio, r_s.

Fig. 2 shows the average ratio of r_t (ρ_{toa2}/ρ_{toa1}, averaged over 15 test areas and 11 images, where ρ_{toa2} is TOA reflectance estimated using OLI TOA radiance product and the different spectral solar constant models, and ρ_{toa1} is the direct TOA reflectance calibrated product). Table III shows the average ratio and its standard deviation. The ratio, which estimates r_t, is temporally stable and showed no variations based on land cover changes (small standard deviation, STD) but only varies between different bands/wavelengths and selections of spectral solar constant model (see Table III). This stability is expected, and the ratios can also be directly estimated and confirmed from the Landsat 8 calibrations as will be shown later.

Fig. 3 shows the average ratio of r_s (ρ_{s2}/ρ_{s1}, where ρ_{s2} is retrieved Lambertian surface reflectance using the TOA radiance product and the different spectral solar constant models, and ρ_{s1} is obtained by using the TOA reflectance product). While generally similar, there are some significant differences

TABLE III
TOA REFLECTANCE RATIO r_t AND STANDARD DEVIATION (STD)

Model	1		2		3		4		5		6	
band	Mean	STD	Mean	STD	Mean	STD	Mean	STD	Mean	STD	Mean	STD
1	1.0589	0.0010	0.9949	0.0006	1.0270	0.0007	1.0470	0.0009	1.0413	0.0009	1.0071	0.0005
2	0.9942	0.0006	0.9802	0.0007	0.9915	0.0006	1.0218	0.0006	1.0053	0.0006	0.9925	0.0005
3	0.9881	0.0005	0.9850	0.0005	1.0066	0.0005	1.0038	0.0005	1.0207	0.0005	0.9972	0.0003
4	1.0028	0.0006	0.9946	0.0006	0.9977	0.0006	0.9963	0.0006	1.0117	0.0006	1.0070	0.0003
5	1.0088	0.0006	1.0003	0.0006	0.9604	0.0005	0.9839	0.0006	1.0088	0.0006	1.0129	0.0004
6	0.9776	0.0005	0.9840	0.0006	0.9837	0.0006	0.9688	0.0006	0.9634	0.0007	0.9963	0.0004
7	0.9774	0.0006	0.9716	0.0007	0.9715	0.0007	0.9712	0.0007	0.9378	0.0013	0.9837	0.0004
Ave	1.0011	0.0006	0.9872	0.0006	0.9912	0.0006	0.9990	0.0006	0.9984	0.0007	0.9995	0.0004

TABLE IV
SURFACE REFLECTANCE RATIO r_s AND STANDARD DEVIATION (STD)

Model	1		2		3		4		5		6	
band	Mean	STD	Mean	STD	Mean	STD	Mean	STD	Mean	STD	Mean	STD
1	1.1957	0.0578	0.9829	0.0061	1.0899	0.0264	1.1564	0.0461	1.1373	0.0404	1.0240	0.0080
2	0.9840	0.0052	0.9456	0.0165	0.9766	0.0075	1.0595	0.0176	1.0143	0.0044	0.9796	0.0068
3	0.9661	0.0180	0.9569	0.0228	1.0186	0.0095	1.0110	0.0059	1.0585	0.0300	0.9928	0.0044
4	1.0079	0.0070	0.9845	0.0118	0.9933	0.0058	0.9893	0.0085	1.0329	0.0251	1.0152	0.0091
5	1.0164	0.0096	1.0003	0.0014	0.9259	0.0447	0.9697	0.0187	1.0164	0.0097	1.0198	0.0087
6	0.9721	0.0077	0.9808	0.0041	0.9801	0.0050	0.9617	0.0096	0.9548	0.0118	0.9957	0.0006
7	0.9730	0.0067	0.9660	0.0088	0.9657	0.0089	0.9659	0.0088	0.9255	0.0190	0.9820	0.0022
Ave	1.0164	0.0160	0.9739	0.0102	0.9929	0.0154	1.0162	0.0164	1.0200	0.0200	1.0013	0.0057

between the results shown in Figs. 2 and 3, primarily in the coastal blue, blue, and green bands. These results can be directly interpreted using (9). In (9), the choice of solar constant affects the retrieved surface reflectance both through r_t and the path radiance bias. The factor $(r_t - 1)$ implies that the bias increases the divergence away from 1.0 with greatest effect in the coastal blue band. Due to the variation of the atmosphere (e.g., aerosol and water vapor), the effects vary with time, leading to significant temporal variation in the visible region. Each band and land cover type creates different temporal and spatial variations. Among specific land cover classes, dark target ratios show the greatest departures from 1.0 when the path radiance bias is high. The results are also shown in Table IV. The standard deviations in Table IV are much higher than those in Table III.

Figs. 2 and 3, therefore, show how even if the deviation of r_t from 1.0 is small, the overall impact for the surface reflectance retrieval can be much larger, especially in dark targets and the far blue end of spectrum. In these situations, selecting a suitable solar constant model is essential to retrieve a reliable surface reflectance from a radiance based product. The use of the OLI TOA reflectance product as reference also allows the "best" model to be defined as the one that leads to the signatures from the OLI radiance product being most similar to those from the OLI reflectance product.

If only Models 1–5 are considered, Fig. 3 and Table IV show that Model 2 is best fitting to the ratio 1.0 in terms of standard deviation, but the r-value still has an overall low bias from 1.0. This conclusion is supported through the analysis of individual scenes and sites. However, it is not as clear in Fig. 2 as it is in the data due to the clustering of the different models. The bias in Model 2 led to the use a value of 0.988, very close to its mean r_t in Table III, as a factor to adjust the TSI of the model. This resulted in a new model (Model 6), which achieves the least bias in all cases and the closest match of results produced from the OLI radiance product to those produced from the OLI reflectance product.

The other models vary much more significantly than Models 2 and 6 – particularly at the blue end of the spectrum. Although the two models based on Thuillier's measurements (Models 3 and 5) perform better in coastal blue band compared with Models 1 and 4, they are variable in other areas of the spectrum and neither performs well in the comparisons made here, suggesting that they may need to be revised.

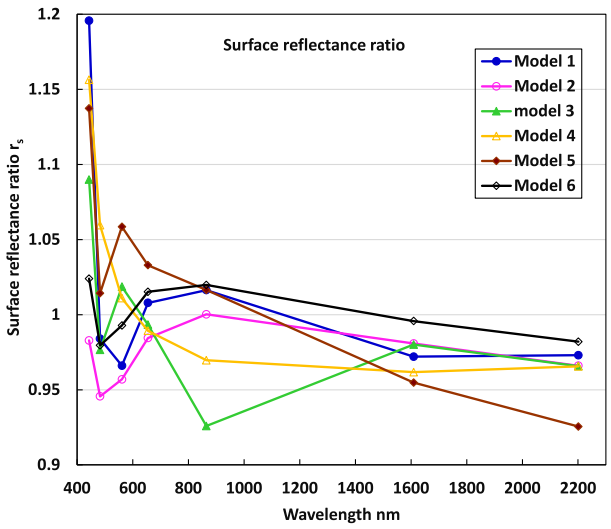

Fig. 4. Average difference $\rho_{s2}-\rho_{s1}$ (average of all valid pixels for 11 images), where ρ_{s2} is retrieved Lambertian surface reflectance using Landsat 8 TOA radiance product and the different spectral solar constant models, and ρ_{s1} is obtained by using Landsat 8 TOA reflectance product.

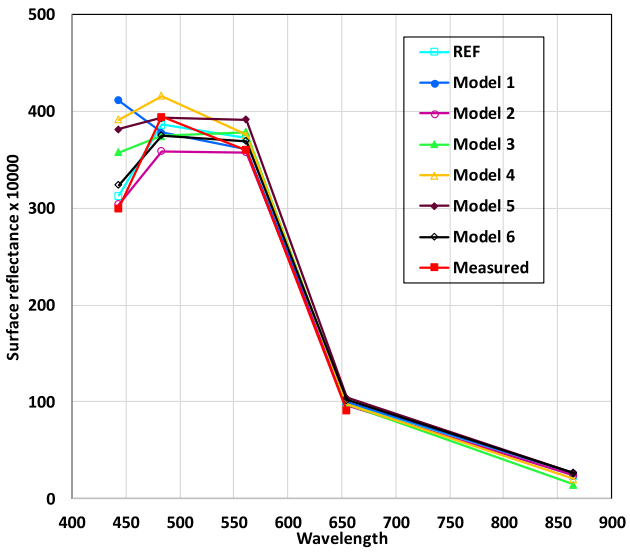

Fig. 5. Comparison between water leaving reflectance retrieved from OLI TOA reflectance and radiance products with different spectral solar constant models and ground measurements on October 2, 2014. "Measured" indicates the CIMEL ρ_w measurement and "REF" means using the TOA reflectance product to retrieve ρ_w. "Model 1"–"Model 6" means ρ_w retrieved using the TOA radiance product with the different spectral solar constant models shown in Table I.

Models 1 and 4 did not perform well in the coastal blue band and have quite divergent properties in different parts of the spectrum. The analysis, therefore, poses some relevant questions in regards to the way these models were constructed.

Figs. 2 and 3 and Tables III and IV only show averages at the 15 selected test sites (yellow stars in Fig. 1). Fig. 4 shows the overall reflectance change ($\rho_{s2}-\rho_{s1}$, average of all valid pixels for 11 images) for different spectral solar constant models. The difference follows (8) with r-values above 1.0 being biased higher and r-values below 1.0 being biased lower. Fig. 4 clearly shows similar patterns to Figs. 2 and 3 with the path radiance bias playing a significant role. Among the various models, the results from using the adjusted Kurucz 2005 model (Model 6) again gave overall best results as measured by the least bias. Models 3 and 5, both of which are based on Thuillier *et al.* [4], gave the highest general divergence. The most noticeable specific variations are in the coastal blue band. The highest divergence in the coastal blue band was for Model 1, which generated a very high surface reflectance with the average difference being over 0.01 reflectance units. This bias in the radiance product has fundamental implications in aquatic applications which use radiative transfer or physics-based approaches, such as for water quality assessment and shallow water bathymetry derivation. Although the influence on the coastal blue band has brought this problem to the fore, this study shows that other regions of the spectrum are also affected.

To increase confidence in the above analysis, the estimated water leaving reflectance values were compared with ground *in situ* measurements from the Lucinda AERONET installation. Fig. 5 shows one comparison for an image sensed on October 2, 2014. For the water leaving reflectance retrieval, additional corrections were also applied to the Landsat 8 OLI data to account for the removal of sky and sun glint as follows:

$$\rho_{\mathrm{s}} = \rho_{\mathrm{w}} + \rho_{\mathrm{gsun}} + \rho_{\mathrm{gsky}}. \tag{10}$$

In (10), ρ_w is the water leaving reflectance factor shown in Fig. 5. ρ_{gsun} and ρ_{gsky} are sun glint and sky glint, respectively. Details as to how ρ_{gsun} and ρ_{gsky} are computed can be found in [18]. Since the estimation of ρ_{gsun} and ρ_{gsky} is independent of the choice of spectral solar constant, the relationship between ρ_{w} and spectral solar constant should be the same as the one between ρ_{s} and spectral solar constant.

The measured ρ_w data obtained by the SeaPRISM instrument located at LJCO, compared with the ρ_w derived from the OLI TOA reflectance and radiance with different spectral solar constant models, are shown in Fig. 5. The diverging results in Fig. 5 are fully consistent with the previous analysis, but, in this case, field data also show how the OLI TOA reflectance product matches the observations the best in magnitude and shape. It is, therefore, clear that if the spectral solar constant model is not selected carefully, not only are the estimates from OLI radiance product noisy but also the retrieved signatures are less accurate, and significantly so for low-reflectance applications such as aquatic remote sensing.

IV. Sensitivity and Error Analysis

In Fig. 3 and Table IV, it can be observed that the ratios of reflectance values at the surface (r_s) from Case 1 and Case 2 in the different bands can depart significantly from the corresponding r-values at TOA r_t. The observed magnitude of the difference in the bands depends on the atmospheric conditions and the land covers sensed. Equation (9) shows how if all r_t values are 1.0, there is no variation between r_s and r_t for any land covers or any atmospheric conditions. The difference of r_t value from 1.0 is, therefore, the major source of differences between surface reflectance values based on the reflectance product from those based on the radiance product in images.

Assume that the difference of r-value from 1.0 is written as $\delta r_t = r_t - 1$ and $\delta r_s = r_s - 1$, then (9) can be rewritten as

$$r_s = \frac{\rho'_{s2}}{\rho'_{s1}} = (1+\delta r_s) = (1+\delta r_t) + \delta r_t \frac{\rho^*_p}{\rho'_{s1}} \tag{11}$$

$$\delta r_s = \delta r_t \left(1 + \frac{\rho^*_p}{\rho'_{s1}}\right). \tag{12}$$

Equation (12) was derived to directly relate the variations of the ratio of reflectance values obtained using the radiance and reflectance products at the surface (r_s) with the r-value at TOA (r_t).

The surface variations δr_s are created by different land covers (ρ'_{s1} which is the reference reflectance in the band being considered) and different atmospheres [ρ^*_p from (7) combines path radiance reflectivity and atmospheric transmittances] and vary with spectral band.

The first thing to note is that for NIR and SWIR bands, the path radiance reflectivity is very small or negligible, and transmittance is large. The variation in the r-value at the surface (δr_s) is, therefore, simply the same as the variation at the TOA (δr_t). The effects on the reflectance at a surface described earlier in this article (such as seen in Fig. 5) are mostly properties of the visible region and are greatest in the coastal blue band because the path radiance reflectivity is largest and the atmospheric transmittances are the least in this band. The offset in (12) alters the ratio of reflectance values most for land covers, where the band reflectance values are small. These are also the situations, where the offset effect is most detrimental to the values obtained using the radiance product. δr_s is, therefore, a very sensitive measure of performance and is clearly determined directly by the magnitude of δr_t.

The studies that have been undertaken in Section II-A and Section III confirmed how the simple model of (12) can precisely describe the variance that occurs between different land covers and when the atmospheric parameters change and how it is modulated by changes in δr_t. Questions as to how changes in atmosphere parameters (e.g., aerosol optical depth) will modify the variation observed in an image can, therefore, be answered directly using (12).

The basic assumption made so far in evaluating the spectral solar constant models has been that the Landst 8 calibrations for the radiance and reflectance products are accurate. If this is relaxed, variations in radiance and/or reflectance calibration will also be present as percentage changes in the r-values. These perturbations can lead to additional misalignment between the selected and "true" spectral solar constant. To evaluate the effects of calibration error on the previous results, it is necessary to establish the relative contributions to δr_t from changing spectral solar constant model and from calibration error.

The calibrations for the radiance and reflectance products in Landsat 8 are made using multiplicative factors. The delivered Landsat 8 metadata provides slope and bias factors for each band and each of two products (reflectance and radiance), for which one finds

$$\text{output} = \text{slope} \times \text{DN} + \text{bias} = \text{slope} \times (\text{DN} - 5000). \tag{13}$$

Defining C_{rad} for the radiance calibration and C_{ref} for the reflectance calibration (basically the reciprocal of the panel reflectance in adjusted DN), then

$$r_t = \frac{\rho_{\text{toa2}}}{\rho_{\text{toa1}}} = \frac{\pi C_{\text{rad}} \times (\text{DN} - 5000)/E'_{02}}{C_{\text{ref}} \times (\text{DN} - 5000)} = \frac{\pi C_{\text{rad}}}{C_{\text{ref}} E'_{02}} = 1 + \delta r_t. \tag{14}$$

Equation (14) shows that r_t does not depend on the DN. The result can, therefore, be computed based on the underlying calibration values or the slopes found in the image metadata file as well as some knowledge of Sun–Earth distances. r_t has previously been shown in Table III for each spectral solar constant model and each spectral band. For Table III, they were computed as averages over all the images for the 15 selected land cover types shown in Fig. 1. The small standard deviations (corresponding to about 0.05% coefficient of variation) show that the underlying calibration coefficients for radiance and reflectance were very stable in the image products used in the study period.

Table V shows the analysis of the δr_t values for the six spectral solar constant models and the seven Landsat 8 bands used in this article. The mean r_t values are taken from Table III and included for reference. In Table V, the column $\delta r_t = r_t - 1$ lists the offset of r_t from 1.0 as introduced above. The mean of the δr_t values for seven Landsat 8 bands indicates bias, the standard deviation of the δr_t values indicates the unbiased variation, and the root mean square (rms) of the δr_t values is the total variation (including bias and standard deviation).

The most significant bias (the mean δr_t in Table V) is for the Model 2. Model 2 was adjusted by a constant multiplier to remove the bias and to get the final Model 6 in this article. The standard deviations of Models 2 and 6 are also effectively the same. Other models do not have as large bias terms, and adjusting them as was done for Model 2 does not make a significant difference. This can be seen from Table V because, for these models, the standard deviation is approximately equal to the rms.

The large values of δr_t in specific bands indicate the potential locations of the problems discussed earlier. The rms of δr_t measures the total rms departure of the given model from r_t of 1.0 in all bands. The order in decreasing magnitude of overall rms for the choices of spectral solar constant model is Model 5 (3.56%), Model 4 (2.82%), Model 1 (2.81%), Model 3 (2.39%), Model 2 (1.62%), and Model 6 (1.01%). The higher the value, the more variation will be seen in images, and the less agreement will be between Landsat 8 surface reflectance values obtained from the radiance product and the equivalent values from the reflectance product.

If C'_{rad} represents the "true" values for a perfect radiance calibration, and C'_{ref} represents the "true" values for a perfect reflectance calibration, the ratio due only to the use of different spectral solar constant models can be written as

$$r_M = \frac{\pi C'_{\text{rad}}}{C'_{\text{ref}} E'_{02}} = 1 + \delta r_M. \tag{15}$$

In this expression, the "M" indicates the selected model for E'_{02}. Furthermore, if errors in the radiance and reflectance calibrations perturb the ratio of the calibration factors by a

TABLE V
TOA REFLECTANCE RATIO r_t AND ITS VARIATION δr_t

Model	1		2		3		4		5		6	
band	*Mean* r_t	δr_t	*Mean* r_t	δr_t	*Mean* r_t	δr_t	*Mean* r_t	δr_t	*Mean* r_t	δr_t	*Mean* r_t	δr_t
1	1.0589	0.0589	0.9949	-0.0051	1.0270	0.0270	1.0470	0.0470	1.0413	0.0413	1.0071	0.0071
2	0.9942	-0.0058	0.9802	-0.0198	0.9915	-0.0085	1.0218	0.0218	1.0053	0.0053	0.9925	-0.0075
3	0.9881	-0.0119	0.9850	-0.0151	1.0066	0.0066	1.0038	0.0038	1.0207	0.0207	0.9972	-0.0028
4	1.0028	0.0028	0.9946	-0.0054	0.9977	-0.0023	0.9963	-0.0037	1.0117	0.0117	1.0070	0.0070
5	1.0088	0.0088	1.0003	0.0003	0.9604	-0.0396	0.9839	-0.0161	1.0088	0.0088	1.0129	0.0128
6	0.9776	-0.0224	0.9840	-0.0160	0.9837	-0.0163	0.9688	-0.0312	0.9634	-0.0366	0.9963	-0.0037
7	0.9774	-0.0266	0.9716	-0.0284	0.9715	-0.0285	0.9712	-0.0288	0.9378	-0.0622	0.9837	-0.0163
Ave	1.0011	0.0011	0.9872	-0.0128	0.9912	-0.0088	0.9990	-0.0010	0.9984	-0.0016	0.9995	-0.0005
STD		0.0281		0.0099		0.0222		0.0282		0.0355		0.0101
RMS		0.0281		0.0162		0.0239		0.0282		0.0356		0.0101

TABLE VI
APPROXIMATE δr_M

Model	1	3	4	5
band	δr_M	δr_M	δr_M	δr_M
1	0.0640	0.0321	0.0521	0.0464
2	0.0140	0.0113	0.0416	0.0251
3	0.0032	0.0217	0.0188	0.0357
4	0.0082	0.0031	0.0017	0.0171
5	0.0085	-0.0399	-0.0164	0.0085
6	-0.0064	-0.0003	-0.0152	-0.0206
7	0.0018	-0.0001	-0.0004	-0.0338

fractional error δC, then the relationship between the above quantities and calculated r_t can be written as $r_t = r_M(1+\delta C)$. It follows that

$$r_t = (1+\delta r_t) = r_M(1+\delta C) = (1+\delta r_M)(1+\delta C) \approx 1 + (\delta r_M + \delta C). \quad (16)$$

The result can be summarized more simply as $\delta r_t = \delta r_M + \delta C$. That is, to a close approximation (neglecting second order perturbations), the fractional differences of r_t from 1.0 can be looked at as the sum of a constant term due to calibration error and a variable term due to using different spectral solar constant models.

Markham *et al.* [11] have demonstrated how Landsat 8 has much higher in-orbit SNR and radiometric fidelity than any previous Landsat instrument. In addition, Morfitt *et al.* [19] showed that radiometric uniformity and stability are within 0.5% in position and time. This means that any present calibration errors are not random variables but rather stable bias terms. As to the possible magnitude of these bias terms, Markham *et al.* [11] quoted it to be 3% in radiance and 2% in reflectance for individual bands. Calibration errors in the reflectance product come from the SNR of the instrument (the solar reference is read by the sensor) and changes in the panel's properties due to exposure to space. SNR may contribute less than 0.5%. Landsat 8 uses two panels, one regularly and the other infrequently to track changes in panel properties. From the stability in reported comparisons of the panel reflectance using both panels [19], it seems possible that the absolute reflectance performance could be better than the 2%.

If some differences in bands are due to the calibration errors (i.e., the δC terms), then, based on the stability reported in [11] and [19], the δC terms must have constant magnitude and sign and not change with the different selections of spectral solar constant models. Moreover, the variations due to the calibration error are independent of the spectral solar constant models and the δr_M terms that they generate. The spectral solar constant models were developed from totally separate information. They may, therefore, be reasonably assumed to be not significantly correlated with them. If uncorrelated, then (approximately) $\mathrm{RMS}(\delta r_t)^2 \approx \mathrm{RMS}(\delta r_M)^2 + \mathrm{RMS}(\delta C)^2$. That is, the rms of perturbation due to the calibration error will be effectively the same and present for each selection of spectral solar constant model.

It follows that if the rms of the constant δC values were large, then no model would align well with the true solar constant as measured from the panel. However, since Model 2 (even without adjustment) aligns very closely (rms < 2%) with the panel data, the overall rms of the constant δC values is presumably no larger than this.

Based on these principals, an estimate for the different components of the variation in r_t can be established. Model 2 is closest to the "true" spectral solar constant having the smallest rms among the five independent solar irradiance models. As Model 6 is a fitted model based on Model 2, it is not included for this analysis. The following relationship holds for differences between δr_t for Model j and Model 2:

$$\delta r_{t_j} - \delta r_{t_2} = \delta r_{M_j} - \delta r_{M_2} \quad (17)$$

where j is the model number, and j can be 1, 3, 4, and 5. In (17), δC cancels out as the calibration error is constant between choices of spectral solar constant model. As Model 2 is close to the "true" solar constant, it will be assumed that equal to it, then $\delta r_{M_2} = 0$. The estimate for δC is then $\delta C =$

δr_{t_2} (see Table V). For the exact perturbations due to models:

$$\delta r_{M_j} = \delta r_{t_j} - \delta r_{t_2} = \delta r_{t_j} - \delta C. \tag{18}$$

This simple solution is approximated as Model 2 is still likely different from the "true" spectral solar constant.

Based on Table V and the above assumptions, an estimate for the calibration errors has an rms 1.62% with the largest band error of 2.84% for band 7. Its size is, therefore, within the bounds quoted in [11] and [19]. It is conservative because if Model 6 was used, the rms would be 1% with the largest band error of 1.63% for band 7. With that choice, the Model 2 rms would be a sum of calibration and solar constant model variations.

Table VI shows the approximate δr_{M_j} values based on Table V and (18). Table VI shows that most of the extreme values that can be observed in Table V are preserved with values again between 3% and 6%. These extremes, which occur in different bands for different models with varying signs, are the primary causes of the problems that have been described in this article.

These observations support the conclusion that if calibration variations are bounded by the orders claimed by Markham *et al.* [11] and Morfitt *et al.* [19], the variations observed between the choices of spectral solar constant model and the effects they have on surface reflectance are primarily due to the model differences. Furthermore, the suggestion that Model 2 aligns best with the reflectance product among the original selected models is consistent with such levels of accuracy, and Model 6 shows that it may be possible to align it even more closely. The results further suggest that the claims made by Markham *et al.* [11] and Morfitt *et al.* [19] for radiance and reflectance calibration accuracy may be conservative.

V. Discussion

Adjusting the fit (or reducing the bias) of Model 2 to obtain Model 6 is similar to modifying the overall TSI of the model. Renormalization can be applied to any of the models used here, but only Model 2 is significantly improved. The TSI of the spectral solar constant certainly will vary with solar activity, and its specific value is important for scientists estimating atmospheric heating. It also varies quite widely among options presented in [7]. In [7], there are seven options (including Model 1 of this article) using model-based studies of solar irradiance by Fontenla *et al.* [3]. These have TSI normalization ranging from 1358.8 to 1361.6 W/m^2 depending on solar activity. The Thuillier-based MODTRAN selection (Model 3 in this article) normalizes to 1376.2 W/m^2, and the Kurucz 2005 (Model 2) normalizes to 1400.5 W/m^2. The adjustment by 0.988 reduces it to 1387.7 W/m^2. The TSI values associated with the Models 4 and 5 used here are unknown. Dewitte and Clerbaux [6] suggested that the long-term observations put the TSI value in the range from 1362 W/m^2 to above 1363 W/m^2. It seems that there are some resolutions needed between these various options. Since the differences may depend more on other areas of the spectrum (especially the UV) than those considered in this article, a study of the narrower and less variable region between 400 and 2600 nm would be useful. However, if any adjustments are made to existing models, it is best if they are made for independent reasons and not by fitting to the variations in the r-value, as the latter may be "fitting" to any small but present calibration errors.

This article selects from independently established spectral solar constant models and determines which is "best" to align the radiance- and reflectance-based Landsat 8 products. The models used are all defined at high spectral resolution and sometimes over all wavelengths. If the only objective was to equate the two products of a single sensor, it may be argued that one should confine the solar constant to broadband values and use the results here to define revised versions of the (integrated) solar constant as ($r_t \times E_{02}$) in each of the Landsat 8 bands. The use of this with a broadband atmospheric correction can certainly make the radiance and reflectance products identical as the new effective $r_t = 1.0$ in each band. The problem is that it is only available for a specific sensor as it uses the sensor bandpass functions, and it cannot generally be modified for use with another sensor. In addition, it incorporates residual calibration errors as they are included in the r_t values. There is no need to use this expression for Landsat 8 as the reflectance product is already available. For other sensors of the Landsat series, there are usually enough differences in bandpass functions between similar bands to make it difficult to transfer the values. The better situation is to find a "best" model for the spectral solar constant from among those that have been defined using independent solar observations at high spectral resolution. This model can then be used for new bandpass functions of new sensors and be independent of any calibration errors in Landsat 8. For scientists who use radiative transfer at fine spectral or wavenumber levels as the basis for atmospheric correction, it is much better to have a satisfactory model defined over all wavelengths involved than only for the broad bandpass functions of a particular sensor. Progress to finding this "best" model would be significantly advanced if hyperspectral sensors with both well-calibrated reference panels and lamp calibrations are launched into orbit.

It would be ideal if the various groups involved in producing the currently available spectral solar constant models could reach a consensus based on the observation data over all of the period of observations using any other relevant ancillary information that can be contributed. This article has shown that, perhaps, the Landsat 8 TOA reflectance estimate based on the two calibrations can help in this process. In the meantime, resolving the large differences between the two models that are (at least in part) based on Thuillier would also be helpful—especially as one is recommended by CEOS [13] for general and consistent use in atmospheric correction. The available models are mostly the composites of different models in different parts of the spectrum. It is possible that issues with the different renormalizations and splicing have occurred when creating the composite models, and this should be investigated further.

VI. Conclusion

When physics-based atmospheric corrections are applied to Landsat 8 OLI optical TOA radiance data using different spectral solar constant models, the resulting surface reflectance

values can vary significantly. Recently, significant variations have been observed for the blue bands over darker targets. Assuming the OLI calibrations are accurate to the levels claimed by Markham *et al.* [11] and Morfitt *et al.* [19], the extent and nature of the variation were measured by comparing the surface reflectance results from different spectral solar constant models with those retrieved from the TOA reflectance product of OLI. The OLI TOA reflectance product is referenced directly to the solar radiation by the on-board solar diffuser panels.

Using the match of the surface reflectance based on TOA radiance to that based on TOA reflectance as the criterion, a set of available spectral solar constant models from various sources was evaluated. It was found that the Kurucz 2005 model [5] performed best as measured by minimum differences between reflectance- and radiance-based product. Its performance was further improved by adjusting its TSI normalization. This choice resulted in the estimated ground reflectance based on TOA radiance best matching those derived from TOA reflectance over all models and at all sites tested. Results for the other models suggest the need for a serious re-evaluation in a number of cases. Sensitivity analyses show how the variation due to choice of spectral solar constant models depends on spectral band, cover type, and atmospheric conditions. The variations in the radiance product also usually represent erroneous signatures – especially for dark targets in the blue bands. The variation only disappears when the selected spectral solar constant aligns closely with the panel observations. The differences due to the selection of spectral solar constant have been shown to be much greater than any that may be due to calibration error given the current accuracy of the Landsat 8 radiance and reflectance products.

The results from this analysis are shown to be particularly relavant for aquatic applications, and especially, to sensors that do not have the kind of direct TOA reflectance measurements now available with Landsat 8 OLI. This class includes the historical collections of Landsat data. With standardized time series of satellite data from different missions being increasingly developed, it is important for there to be consistency in preprocessing such as with atmospheric correction. To underpin this aim, it is proposed that an accepted common selection of spectral solar constant should be established and suggested that the Landsat 8 OLI instrument provides ideal data sets to evaluate candidate models.

ACKNOWLEDGMENT

This article is published with the permission of the CEO, Geoscience Australia. The MODTRAN 6 radiative transfer software was used in calculations, and information is taken from the User Manual [7]. Level 1C Landsat 8 images were from United States Geological Survey (USGS).

REFERENCES

[1] C. Fröhlich, "Solar irradiance variability," in *Solar Variability and Its Effects on Climate* (Geophysical Monograph Series), vol. 141. Washington, DC, USA: AGU, 2004, pp. 97–110.

[2] I. Ermolli *et al.*, "Recent variability of the solar spectral irradiance and its impact on climate modelling," *Atmos. Chem. Phys.*, vol. 13, no. 8, pp. 3945–3977, Apr. 2013, doi: 10.5194/acp-13-3945-2013.

[3] J. M. Fontenla, J. Harder, W. Livingston, M. Snow, and T. Woods, "High-resolution solar spectral irradiance from extreme ultraviolet to far infrared," *J. Geophys. Res.*, vol. 116, no. 20, 2011, Art. no. D20108, doi: 10.1029/2011JD016032.

[4] G. Thuillier *et al.*, "The solar spectral irradiance from 200 to 2400 nm as measured by the SOLSPEC spectrometer from the Atlas and Eureca missions," *Sol. Phys.*, vol. 214, no. 1, pp. 1–22, 2003, doi: 10.1023/A:1024048429145.

[5] K. Chance and R. L. Kurucz, "An improved high-resolution solar reference spectrum for Earth's atmosphere measurements in the ultraviolet, visible, and near infrared," *J. Quant. Spectrosc. Radiat. Transf.*, vol. 111, no. 9, pp. 1289–1295, Jun. 2010, doi: 10.1016/j.jqsrt.2010.01.036.

[6] S. Dewitte and N. Clerbaux, "Measurement of the Earth radiation budget at the top of the atmosphere—A review," *Remote Sens.*, vol. 9, no. 11, p. 1143, Nov. 2017, doi: 10.3390/rs9111143.

[7] A. Berk *et al.* (2017). Modtran 6.0 user's manual. Spectral Sciences and Air Force Research Laboratory. [Online]. Available: http://modtran.spectral.com/

[8] L. Zhang, S. Hu, H. Yang, T. Wu, Q. Tong, and F. Zhang, "The effects of solar irradiance spectra on calculation of narrow band top-of-atmosphere reflectance," *IEEE J. Sel. Topics Appl. Earth Observ. Remote Sens.*, vol. 7, no. 1, pp. 49–58, Jan. 2014, doi: 10.1109/JSTARS.2013.2265751.

[9] K. J. Thome, S. F. Biggar, and P. N. Slater, "Effects of assumed solar spectral irradiance on intercomparisons of Earth-observing sensors," *Proc. SPIE*, vol. 4540, pp. 260–269, Dec. 2001, doi: 10.1117/12.450668.

[10] P. Shanmugam and Y. H. Ahn, "Reference solar irradiance spectra and consequences of their disparities in remote sensing of the ocean colour," *Annales Geophysicae*, vol. 25, no. 6, pp. 1235–1252, Jun. 2007, doi: 10.5194/angeo-25-1235-2007.

[11] B. Markham *et al.*, "Landsat-8 operational land imager radiometric calibration and stability," *Remote Sens.*, vol. 6, no. 12, pp. 12275–12308, Dec. 2014, doi: 10.3390/rs61212275.

[12] E. F. Vermote, D. Tanre, J. L. Deuze, M. Herman, and J.-J. Morcette, "Second simulation of the satellite signal in the solar spectrum, 6S: An overview," *IEEE Trans. Geosci. Remote Sens.*, vol. 35, no. 3, pp. 675–686, May 1997, doi: 10.1109/36.581987.

[13] *CEOS Recommended Solar Irradiance Spectrum for Use in Earth Observation Applications*. Accessed: 2019. [Online]. Available: https://eocalibration.wordpress.com/2006/12/

[14] N. Pahlevan, Z. Lee, J. Wei, C. B. Schaaf, J. R. Schott, and A. Berk, "On-orbit radiometric characterization of OLI (Landsat-8) for applications in aquatic remote sensing," *Remote Sens. Environ.*, vol. 154, pp. 272–284, Nov. 2014, doi: 10.1016/j.rse.2014.08.001.

[15] G. Zibordi *et al.*, "AERONET-OC: A network for the validation of ocean color primary products," *J. Atmos. Ocean. Technol.*, vol. 26, no. 8, pp. 1634–1651, Aug. 2009, doi: 10.1175/2009JTECHO654.1.

[16] F. Li, *et al.* "An evaluation of the use of atmospheric and BRDF correction to standardize Landsat data," *IEEE J. Sel. Topics Appl. Earth Observ. Remote Sens.*, vol. 3, no. 3, pp. 257–270, Sep. 2010, doi: 10.1109/JSTARS.2010.2042281.

[17] *Lucinda AERONET Data*. Accessed: 2019. [Online]. Available: https://aeronet.gsfc.nasa.gov/cgi-bin/type_one_station_seaprism_new?site=Lucinda&nachal=2&level=1&place_code=10

[18] F. Li, D. L. B. Jupp, S. Sagar, L.-W. Wang, and R. Coghlan, "Atmospheric correction for a Landsat and Sentinel-2 product over water surfaces," in *Proc. 22nd Int. Congr. Modelling Simulation*, Hobart, TAS, Australia, Dec. 2017, pp. 971–977. [Online]. Available: mssanz.org.au/

[19] R. Morfitt *et al.*, "Landsat-8 operational land imager (OLI) radiometric performance on-orbit," *Remote Sens.*, vol. 7, no. 2, pp. 2208–2237, Feb. 2015, doi: 10.3390/rs70202208.

Fuqin Li (Senior Member, IEEE) received the Ph.D. degree in atmospheric science from Murdoch University, Murdoch, WA, Australia, in 2001.

She was a Research Scientist with the Chinese Academy of Sciences Institute of Remote Sensing Applications (IRSA), Beijing, China, until 1995. From 2002 to 2008, she was a Physical Scientist with USDA Hydrology and Remote Sensing Laboratory, Beltsville, MD, USA. She is a Senior Calibration Specialist with Analysis Ready Data team within Digital Earth Australia program at Geoscience Australia, Canberra, ACT, Australia. Her research interests include physically based atmospheric, BRDF, and terrain illumination corrections for satellite data, evapotranspiration, and water balance models using remote sensing as well as data assimilation.

David L. B. Jupp (Life Member, IEEE) received the Ph.D. degree in applied mathematics from Flinders University, Adelaide, SA, Australia, in 1973.

Since 1976, he has been worked at CSIRO (Australia) with special interests in remote sensing. He is a Post-Retirement Fellow with CSIRO Land and Water, Canberra, ACT, Australia. His research interests include in hyperspectral and lidar remote sensing of vegetation, satellite calibration and validation, and physical models for land covers and imaging. He was formerly Science Leader, CSIRO Earth Observation Centre (EOC). Previous applications have been to coastal zone (including reefs) and inland waters; thermal data analysis of land surface temperature for soil moisture and water balance. Commercialisation has included an early PC-based image processing system, software for airborne spectrometer data and more recently the development of a ground-based lidar system for vegetation mapping.

Stephen Sagar received the Ph.D. degree in Earth physics from the Australian National University, Canberra, ACT, Australia, in 2015.

He leads the aquatic product development team within the Digital Earth Australia (DEA) program at Geoscience Australia, Canberra, ACT, Australia. The team delivers innovative time-series Earth observation capabilities for government stakeholders in the aquatic and marine space, leveraging a rich archive of publically available data sources. He examining probabilistic approaches and uncertainty analysis in shallow water radiative transfer applications and inversion problems. His research is focused on the application and development of remote sensing algorithms in coastal, shallow water and inland water environments; most recently to address the complexity of remote sensing in the intertidal zone.

Thomas Schroeder received the M.Sc. degree in meteorology in 2001 and was awarded the Ph.D. degree in 2005 from the Department of Earth Sciences, Free University Berlin, Berlin, Germany.

He worked as a Research Scientist with the Institute of Space Sciences, Free University Berlin, until 2005 before he took up employment with the German Aerospace Centre DLR, Oberpfaffenhofen, Germany. In 2006, he moved to Australia, where he works as a Senior Research Scientist with the Ocean and Atmosphere Coasts Program. His research focuses on the development, validation, and implementation of physics-based ocean color inversion algorithms for Australia's coastal and marine ecosystems using multi- and hyper-spectral satellite data to enable reliable mapping, detection and monitoring of aquatic resources. Furthermore, he is progressing new strategic research directions in the area of geostationary and radar satellite applications for high-temporal coastal monitoring and the detection of hydro-carbon pollution. He is also advancing *in situ* bio-optical and radiometric observations for satellite validation under the Australian Integrated Marine Observing System (IMOS), where he leads the IMOS Ocean Color Subfacility and manages the Lucinda Jetty Coastal Observatory. Measurements from this facility are used to inform international space agencies on the accuracy of marine satellite products.